

Article

The Enhancement in Optical Characteristics of Nano-Antenna Arrays through Addition of Inverse Active Core–Shell Nanoparticles in the Array Element

Qaisar Hayat ¹, Junping Geng ^{1,*}, Chaofan Ren ¹, Han Zhou ¹, Kun Wang ¹, Atta Ur Rahman ^{1,2}, Silei Yang ¹, Jingzheng Lu ¹, Xianling Liang ¹, Chong He ¹ and Ronghong Jin ¹

¹ Department of Electronics Engineering, Shanghai Jiao Tong University, Shanghai 200240, China

² Department of Physics, Khushal Khan Khattak University, Karak 28420, Pakistan

* Correspondence: gengjunp@sjtu.edu.cn

Abstract: We demonstrate analytically the technique and arrangement of nanoparticle antenna arrays with the enhancement of optical characteristics at an optical frequency regime. The optical characteristics of the array are enhanced by introducing an inverse active spherical coated nanoparticle (I-CNP). This inverse active spherical coated nanoparticle is designed and combined with already demonstrated active CNPs. Consequently, three types of active CNPs and their inverse-based plasmonic nano-antenna array configurations have been designed and studied: two CNP configurations, two inverse CNP (I-CNP) configurations and a CNP with an I-CNP configuration in the presence of passive elements. Detailed near-field analysis contains an E-field, radiated power, scattering and absorption examination, whereas far-field analysis includes gain and pattern investigation. The finite-difference time-domain (FDTD) simulation results in CST depict the benefits of a CNP with an I-CNP array configuration in the presence of passive elements over the other two in terms of both near-field and far-field characteristics, at closer inter-element distances because of coupling avoidance with possession of a dipolar pattern.

Keywords: plasmonic nano-antenna; terahertz photonics; array configuration; nanoparticle; core–shell nano-antenna



Citation: Hayat, Q.; Geng, J.; Ren, C.; Zhou, H.; Wang, K.; Rahman, A.U.; Yang, S.; Lu, J.; Liang, X.; He, C.; et al. The Enhancement in Optical Characteristics of Nano-Antenna Arrays through Addition of Inverse Active Core–Shell Nanoparticles in the Array Element. *Electronics* **2022**, *11*, 2987. <https://doi.org/10.3390/electronics11192987>

Academic Editor: Francesco Giuseppe Della Corte

Received: 23 July 2022

Accepted: 26 August 2022

Published: 21 September 2022

Publisher's Note: MDPI stays neutral with regard to jurisdictional claims in published maps and institutional affiliations.



Copyright: © 2022 by the authors. Licensee MDPI, Basel, Switzerland. This article is an open access article distributed under the terms and conditions of the Creative Commons Attribution (CC BY) license (<https://creativecommons.org/licenses/by/4.0/>).

1. Introduction

Optical antennas are the new concept in physical optics and are the analogues of radio-wave and microwave antennas. The advancement in these optical antennas enables modern technologies to manipulate and control optical radiation at subwavelength scales [1]. Regardless of the prevalent use of radio- and microwave antennas, these optical analogous antennas have not been developed so far in technological applications because of their small sizes and difficult fabrication techniques. These optical antennas are mostly based on the plasmonic effect, which is one of the rapidly growing research areas from the past two decades due to its wide range of applications in solar energy harvesting, biosensors, imaging, medicine, quantum computing, spectroscopy and optical communication [2–4]. Many researchers have designed different plasmonic nano structures for different applications. For example, [5] has presented nanowire waveguides for deep subwavelength confinement. The authors in [6] prepared metallic nanowires for ultrasensitive deflection sensing. In [7–9], the authors showed the coaxial lithography for optical and electrical properties of heterogeneous nanowires. In addition, [8] showed the metal–semiconductor interface for lithography.

Among the applications of plasmonics, the novel optical properties such as resonant scattering and transparency are achievable from active core–shell nanoparticles for nano-sensor applications [10]. These plasmonic-based core–shell nanoparticles also have possible applications as a localized optical sensor [10,11] used in biomedical sensing and imaging.

Due to the tunability of plasmonic resonance in an optical regime [12], these core-shell nano-antennas have potential use in displays. The exciting application of these plasmonic core-shell nano-antennas is their potential to be used in drug delivery [13,14] and cancer therapy [15–17]. In addition to this, these core-shell nano-antennas have the ability to enhance the light-trapping behavior of solar cells and consequently can improve the conversion efficiency of solar cells [18,19]. These plasmonic core-shell nanomaterials also have several advantages over organic dye markers and quantum dots because they have chemical stability, low toxicity and a high signal-to-noise ratio [20].

The spherical core-shell nano-antennas presented to date are of two types, i.e., passive and active nano-antennas [21]. Many numerical and experimental works have been presented on passive core-shell nano-antennas, such as Ag-coated SiO₂ nano-antennas [20,22–25], unidirectional scattering by magneto-electric core-shell nanoparticles [26], a gold nanoparticle-based core-shell [27] and self-assembled 3D arrays of Au-SiO₂ core-shell nanoparticles [28]. Likewise, some active core-shell nanoparticle antennas have been presented purely based on simulations, e.g., active cylindrical and active coated nanoparticles [29], scattering from active core-shell nanoparticles [21,30,31], active coated nano-toroid antennas [32], core-shell arrays with more stability [33] and plasmonic-induced polarization rotation [34]. Some of these arrays of core-shell nanoparticles work out the enhancement of the optical characteristics, such as what is presented in references [29,32,33,35]. Unfortunately, all the active core-shell arrays, as well as the passive core-shell arrays, experience the problem of instability, as the basic units reported till now are placed in open air or in an aqueous solution [27,28,36,37]. However, when a dielectric occupies the spacing between CNPs to achieve stability, the destructive coupling then limits the enhancement of optical characteristics [33]. Similarly, the arrangement of nanoparticles to construct an array for enhancing their optical properties is another issue faced by both passive and active core-shell nano-antennas [33,34,38]. However, the optical properties still need enhancement for applications in nano-sensors and nano-amplifiers.

This article proposes an inverse model of the already proposed active coated nanoparticle (CNP) [34], having silver in the core while the gain medium is in the shell; hence, it is named an active inverse coated nanoparticle (I-CNP). This active I-CNP is then combined with an active CNP and having a dielectric in between them hence constructs a new model. The optical properties of this model are compared at first with the model comprising two active CNPs having a dielectric in between them and with the model comprising two I-CNPs having dielectrics between them. A remarkable enhancement is observed for this mixed model of an active CNP with an active I-CNP in the presence of a dielectric. The dielectric is inserted in all the proposed models for achieving stability, while the size of the dielectric is optimized for the better far-field dipole pattern of scattered radiation. After comparison of the optical properties of the three models, the proposed model is extended two-dimensionally to observe its optical properties. Fortunately, the proposed model does not affect the radiating polarization of the far field. This is because the dielectric is not in a resonant state at the desired frequency when the CNPs and I-CNPs are in a resonant state.

It is important to mention here that a single active CNP may have better optical characteristics over an I-CNP, but the compacted array comprising only active CNPs [33] or I-CNPs (shown in this article) faces large side beams due to the coupling inside the configuration, which limits the gain enhancement of the nanoparticle array, so we called it destructive coupling. Here, this research proposes that the destructive coupling is tailorable and can be decreased by combining the active CNP with I-CNP for both smaller and larger spacing between CNPs and I-CNPs. The combined structure of the CNP and I-CNP actually tailors the electric currents that orient in such directions to obey Kirchhoff's current law, which consequently produces electric fields in such directions to support each other, hence decreasing the destructive coupling and achieving array gain to strengthen the SCS.

2. Modeling the Materials

The optical characteristics are characterized here by scattering cross-section and absorption cross-section, which can be obtained by exciting the core-shell nanoparticles with an electromagnetic planewave [19]. Therefore, we use CST post-processing tools utilizing CST Microwave Studio, which solves Maxwell's equations using the frequency domain method, to calculate these values of scattering and absorption cross-sections. The basic units of the configurations in this research are the spherical active coated nanoparticle (CNP) and the inverse spherical active coated nanoparticle (I-CNP). In CNP model, the erbium-doped silicon dioxide (called an active/gain medium or active SiO₂) shell surrounds silver (Ag) in the core, whereas in I-CNP model, the silver in the shell surrounds the active SiO₂ core.

The boundary condition is open and space in all directions. The mesh size and density affect the convergence of the simulation, and here the final meshes are optimized as minimum step of mesh is 5.0.

2.1. Size-Dependent Drude Model

The silver (Ag) used here is based on the size effect Drude model at optical wavelengths between 200 nm and 1800 nm. The optical response of nano-dimensional materials is tremendously different from their bulk counterpart. The relation given below provides the dielectric response of a material in terms of Drude response and inter-band transition [30,35].

$$\varepsilon_{Drude}(R, \omega) = 1 - \frac{\omega_p^2}{\Gamma(R)^2 + \omega^2} + j \frac{\Gamma(R)^2 \omega_p^2}{\omega(\Gamma(R)^2 + \omega^2)} \quad (1)$$

Here, R , ω_p and Γ represent the thickness of the surrounding shell, the plasma frequency and the collision frequency, respectively.

The values of all Drude parameters and Fermi velocity, used to compute the dielectric dispersion for 10 nm thick silver shell and 58 nm dielectric core, are $m^*/m = 0.96$, $N = 5.85 \times 10^{28} \text{ m}^{-3}$, $V_F = 1.39 \times 10^6 \text{ m/sec}$ and $\omega_p = 1.39269 \times 10^{13} \text{ s}^{-1}$, as given in reference [29]. The separation gap of CNPs and I-CNPs in all three configurations is enough large to prevent quantum tunneling or charge transfer between CNPs; therefore, the size effect in classical Drude model is termed a semi-classical model.

2.2. Lorentz Model for Gain Medium

The gain media in core of CNP and in shell of I-CNP have rare-earth-doped SiO₂. The values for gain media used in CNPs and in I-CNPs are the same as discussed in references [29,35,39]. The following relation describes Lorentz model to incorporate the canonical gain media in CST Microwave Studio.

$$\varepsilon_r(\omega) = \varepsilon_\infty + \frac{(\varepsilon_s - \varepsilon_\infty)\omega_0^2}{\omega_0^2 + j\omega\Gamma - \omega^2} \quad (2)$$

The relative epsilon of the dielectric (silicon dioxide) is set as constant $\varepsilon_r = 2.05$ due to its low loss characteristics, resulting in the refractive index $n = \sqrt{\varepsilon_r} = 1.432$. The optimal value for $k = -0.25$ is set for resonance frequency $f = f_0 = 600 \text{ THz}$ and also $\omega = \omega_0 = 2\pi f_0$ to obtain ε_∞ and then obtain ε_s .

$$\varepsilon_\infty = 1.9875 \text{ and } \frac{(\varepsilon_s - \varepsilon_\infty)\omega_0^2}{\Gamma} = 2nk \quad (3)$$

Re-arrange Equation (2) and replace ε_∞ with its value to obtain:

$$\varepsilon_s = \frac{2nk\Gamma}{\omega_0^2} + 1.9875 \quad (4)$$

The damping frequency Γ is related to the resonance frequency and valued in the range ($10^{-3} \sim 10^{-1}$) ω_0 to represent low to high loss materials listed in [29,39].

2.3. Planewave Excitation

Scattering cross-section (SCS) and absorption cross-section (ACS) can characterize the behavior of core-shell nanoparticles excited by electromagnetic planewaves. SCS is the integrated power enclosed in the scattered field normalized by the irradiance of the incident field, whereas ACS is the measure of the net power flux through a surface surrounding the concentric shells normalized by the incident field irradiance. Therefore, ACS is a measure of how much energy is being absorbed by the concentric shell structure. The scattered and absorbed power can be expressed by the following expression via Poynting's theorem:

$$P_{scat} = Re \left\{ \frac{1}{2} \iint_s \left[\vec{E}_s \times \vec{H}_s^* \right] \cdot \hat{n} dS \right\} \quad (5)$$

$$P_{abs} = -Re \left\{ \frac{1}{2} \iint_s \left[\vec{E}_{tot} \times \vec{H}_{tot}^* \right] \cdot \hat{n} dS \right\} \quad (6)$$

where S is the surface enclosing the particle, and \hat{n} is the unit vector pointing outward to the surface. The total SCS, ACS and ECS can be defined by ratio of radiated power with incidence irradiance.

$$\sigma_{scat} = \frac{P_{scat}}{I_{inc}} \quad (7)$$

$$\sigma_{abs} = \frac{P_{abs}}{I_{inc}} \quad (8)$$

$$\sigma_{ext} = \sigma_{scat} + \sigma_{abs} \quad (9)$$

The values of σ_{scat} , σ_{abs} and σ_{ext} are readily calculated with the CST post-processing tools.

2.4. Designed Single Core-Shell Parameters

The two basic active coated nanoparticle models construct three different configurations for comparison. The first basic CNP model shown in Figure 1a is comprised of silver in the shell of thickness " $R_1 = 10$ nm", and its core is filled with active silica of diameter " $d_1 = 70$ nm"; hence, it constructs an active coated nanoparticle (CNP). Likewise, the second model in Figure 1b consists of a silver core of diameter " $d_2 = 94$ nm" enclosed by an active silica shell of thickness " $R_2 = 60$ nm". Consequently, this formulation becomes the inverse of the first CNP model, i.e., active spherical inverse coated nanoparticle (I-CNP). The resonance peaks of silver (Drude model) and active gain media were firstly optimized at a resonance frequency range of $f_0 = 600$ THz, and then the maximum optimized thickness and diameter are selected for further simulations. These basic models further constitute three different array configurations.

2.5. Designed Parameters of the Three Configurations

In the first configuration, two active CNPs are alienated by a distance of $\lambda/2$ from their centers, as shown in Figure 1c. The parameters of CNPs are optimized with reference to the resonance frequency. As a result, the optimized thickness of the Ag layer in a shell is the same as for a single CNP, i.e., $R_1 = 10$ nm, and the diameter of active silica in the core is $d'_1 = 58$ nm. The passive silica of diameter $L'_1 = 172$ nm fills here the separation between both CNPs. In the second configuration, another passive silica of diameter $L'_2 = 36$ nm combines two I-CNPs by separation of $\lambda/2$ from their centers. The parameters of I-CNPs in Figure 1b and in Figure 1d are the same, i.e., thickness of active silica shell is $R_2 = 60$ nm, and the diameter of the silver core is $d_2 = 94$ nm. Finally, in the third configuration, as shown in Figure 1e, the passive silica of diameter $L'_3 = 104$ nm combines the CNP and

I-CNP with separation $\lambda/2$. Here, the parameters of CNP and I-CNP are the same, as demonstrated in configurations I and II in Figure 1c,d.

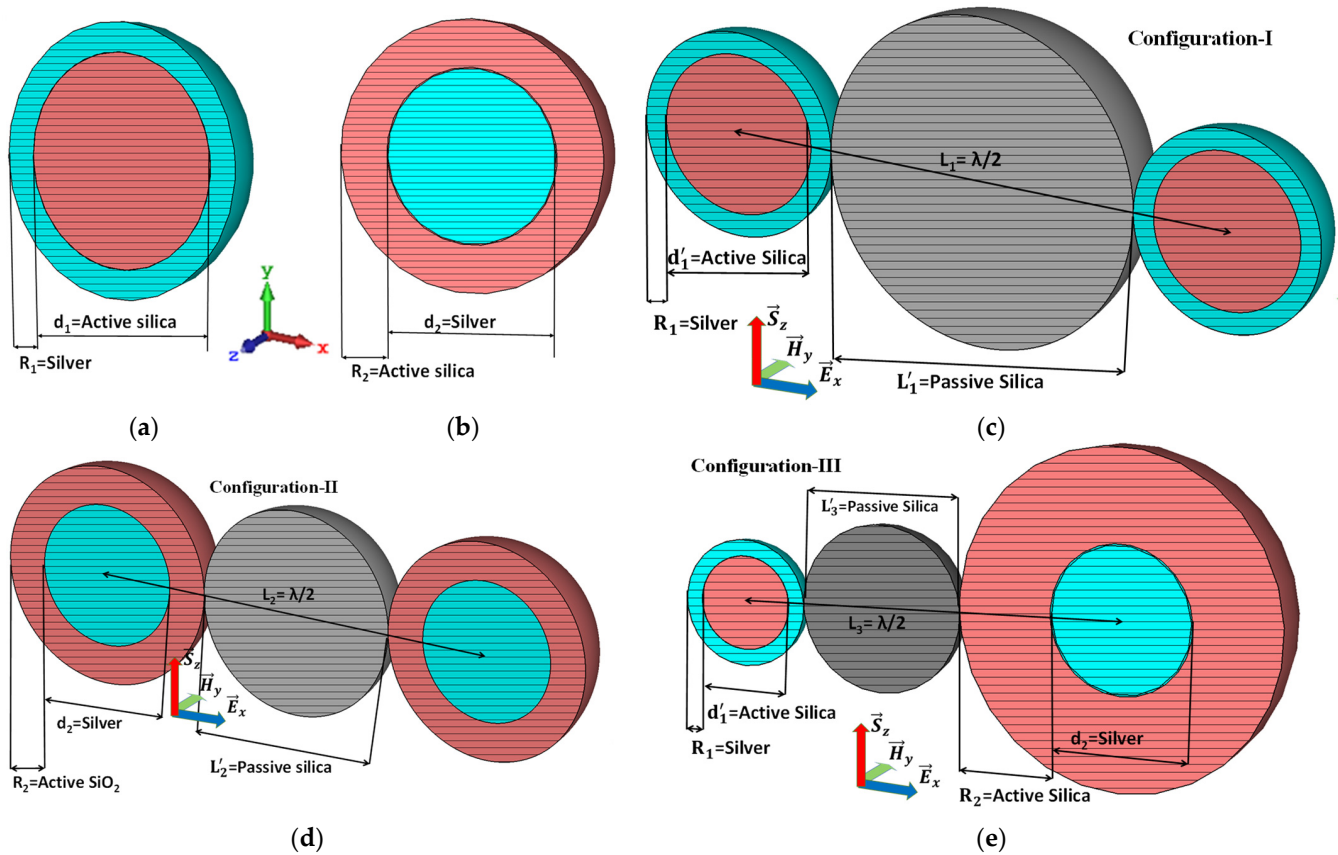


Figure 1. (a) CNP model where a silver shell of thickness $R_1 = 10$ nm encloses the core of active silica of diameter $d_1 = 70$ nm; (b) I-CNP model. The shell of active silica has a thickness of $R_2 = 60$ nm, and the silver core has a diameter of $d_2 = 94$ nm; (c) two CNPs separated by passive silica of diameter $L'_1 = 172$ nm; (d) two I-CNPs separated by passive silica of diameter $L'_2 = 36$ nm; (e) CNP and I-CNP separated by passive silica of diameter $L'_3 = 104$ nm.

2.6. Optimization of Single Core–Shell Parameters

Both the radius and core material are optimizable regarding the performance of the CNP throughout the visible regime. For a constant thickness of silver in the shell, the variance in core diameter changes the resonance frequency peak of the CNP. For example, increase in core diameter shifts the resonance peak of CNP towards lower frequency and vice versa. The optimization of I-CNP follows the same process, where the variations in shell thickness keep the resonance peak variant. Here, the selected thickness of silver (Drude model) and diameter of active SiO₂ were first optimized in CST through simulations. For this purpose, different diameters of active SiO₂ were optimized at desired resonance frequency $f_0 = 600$ THz, while the thickness of shell was kept constant (silver peak is adjusted at resonance frequency $f_0 = 600$ THz), as shown in Figure 2a. Similarly, in the case of I-CNP, the diameter of the silver core is constant, whereas the thickness of gain media in shell is optimized to the desired resonance frequency, as shown in Figure 3a.

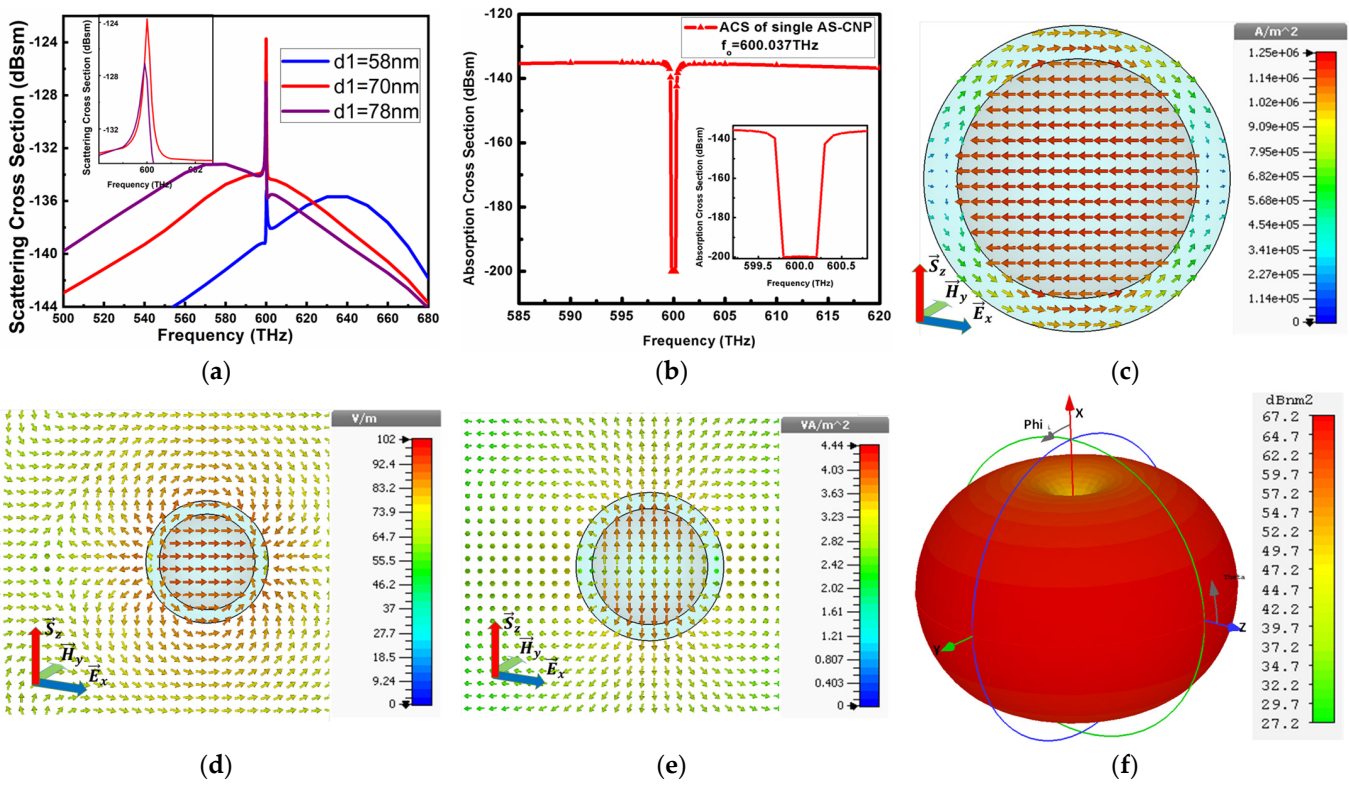


Figure 2. (a) SCS peak, (b) ACS value, (c) electric current density, (d) electric field pattern, (e) power flow pattern and (f) far-field pattern at resonance frequency for individual CNP model.

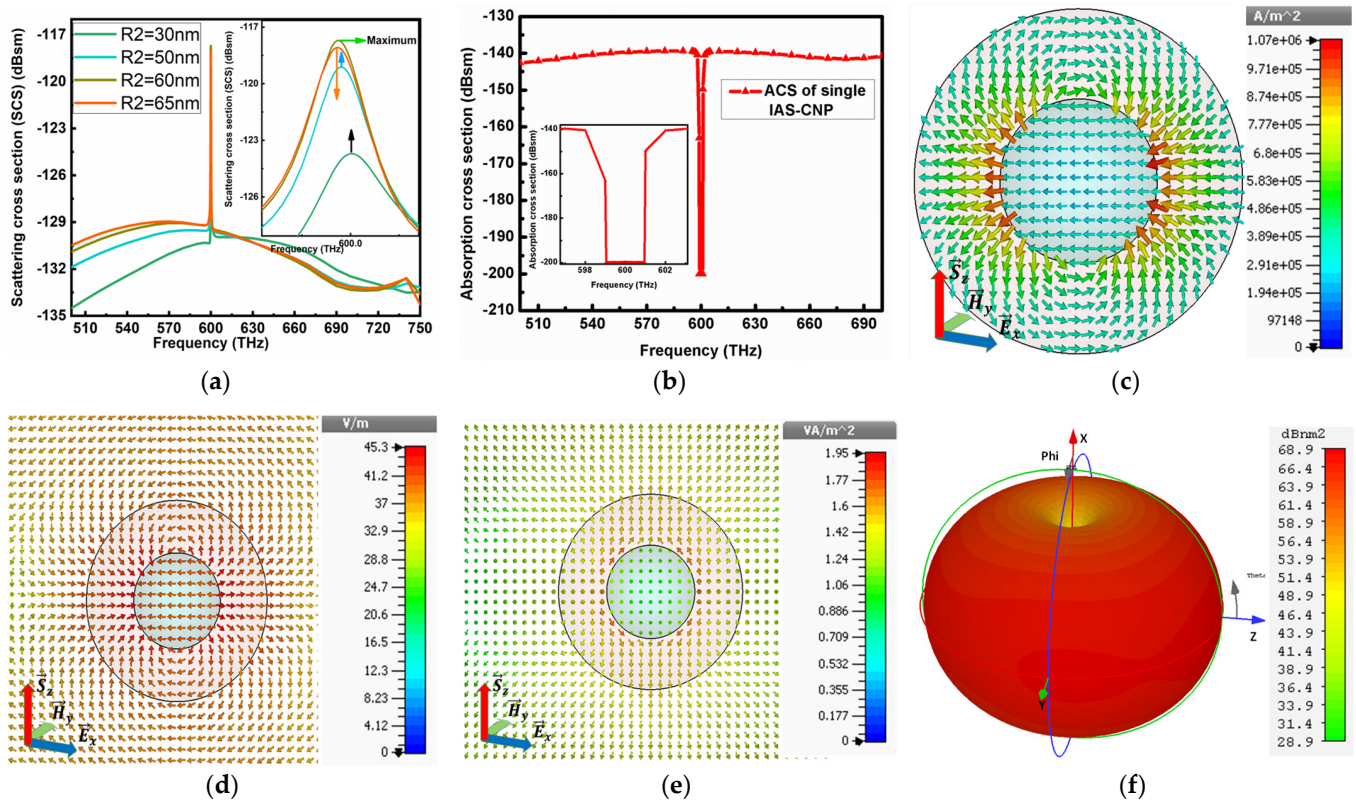


Figure 3. (a) SCS peak, (b) ACS peak, (c) electric current density, (d) electric field pattern, (e) power flow pattern and (f) far-field pattern at resonance frequency for individual I-CNP model.

3. Single Active CNP and I-CNP Results for Planewave Excitation

The \vec{E}_x polarized planewaves propagating in the \vec{S}_z direction excite the individual CNP and I-CNP models at first to obtain their optimized scattering cross-section, absorption cross-section, electric field pattern, power flow and far-field pattern at resonance frequency. The amplitude of this incident planewave is $E_0 = 1.0$ V/m and can be express as:

$$\vec{E} = \hat{x}E_0 \cos(\omega t + kz)$$

Figure 2 shows the labeled diagram of CNP whose similar design is discussed in references [33,34] but for a different thickness of shell and its respective core diameter. Here, a different shell thickness of the CNP is simulated according to the requirements that are explained in detail in Figure 2.

Table 1 shows the optical properties of an individual CNP at $f_0 = 600.037$ THz resonance frequency when excited by \vec{E}_x polarized planewave, whereas Figure 2 gives the diagrammatical illustration of the optical properties shown in Table 1. Here, the scattering cross-section peak, shown in Figure 2a, is -124.66 dBsm, which is 10 dB higher than the ground value, whereas the minimum absorption cross-section reported in Figure 2b is -200 dBsm, which is 65 dB lower than the ground value.

Table 1. Optical properties of the single basic active CNP.

Optical Parameter	Single CNP	Single I-CNP
Thickness of shell	10 nm	60 nm
Core diameter	70 nm	94 nm
Frequency	$f_0 = 600.035$ THz	$f_0 = 600.0335$ THz
SCS max.	-124 dBsm	-117.228 dBsm
ACS below background values	-200 dBsm	-200 dBsm
RCS (far field)	67 dBnm ²	68.9 dBnm ²
E-field (near field)	102 V/m	45.3 V/m
Power flow (max.)	4.44 VA/m ²	1.95 VA/m ²

The current density in Figure 2c is 1.25×10^6 A/m², whereas the electric field in Figure 2d is 102 V/m. Similarly, the arrows in Figure 2e denote 4.4 VA/m² power generating from the center of the CNP flowing towards and away from the source planewave direction. In addition to this, the far-field pattern in Figure 2f supports the power flow along the z-axis, providing a dipole pattern of 67.2 dBnm² gain.

The selection of frequency interval and numerical analysis are the same as for the CNP, as the expected resonance frequency is $f_0 = 600$ THz. Figure 3a,b depicts the scattering cross-section and absorption cross-section of I-CNP when excited by planewaves. The peak SCS reported in Figure 3a is -117 dBsm, which is 13 dB higher than the ground value and again is very close to the anticipated resonance frequency $f_0 = 600.0335$ THz. On the other hand, the ACS reported by Figure 3b is -200 dBsm, which is 50 dB below the background value.

Figure 3c–f elaborates the predicted numerical results of the current density, electric field, power flow and far-field pattern, respectively. The highest current density at the resonant state presented in Figure 3c is 1.07×10^6 A/m², while the stated electric field is 45.3 V/m in Figure 3d. The resonant dipole field in the I-CNP pushes power out of its y-axis, i.e., from the center, and pulls it towards the source side, forming vortices around its poles. In addition to this, the radiated power from the center of the I-CNP is 1.95 VA/m², as publicized in Figure 3e at a resonance frequency of $f_0 = 600.0335$ THz. Similarly, the strong dipole realizes 68.9 dBnm² gain at the resonance frequency shown by the far-field pattern in Figure 3f.

4. Results Comparison for Array Configurations

The \vec{E}_x polarized planewave excites the three configurations, sketched in Figure 1c–e, to compare their optical characteristics near the desired resonance frequency.

When a passive dielectric of $\lambda/2$ size combines the two CNPs (configuration I), the resonance frequency of the CNPs then displaces from the desired frequency. Therefore, to bring the resonance states of both CNPs at the desired frequency, we optimize the size of the gain media in the core of the CNPs. The SCS peaks in Figure 4a show the optimization of gain for configuration I, where the optimized size of the core is 58 nm.

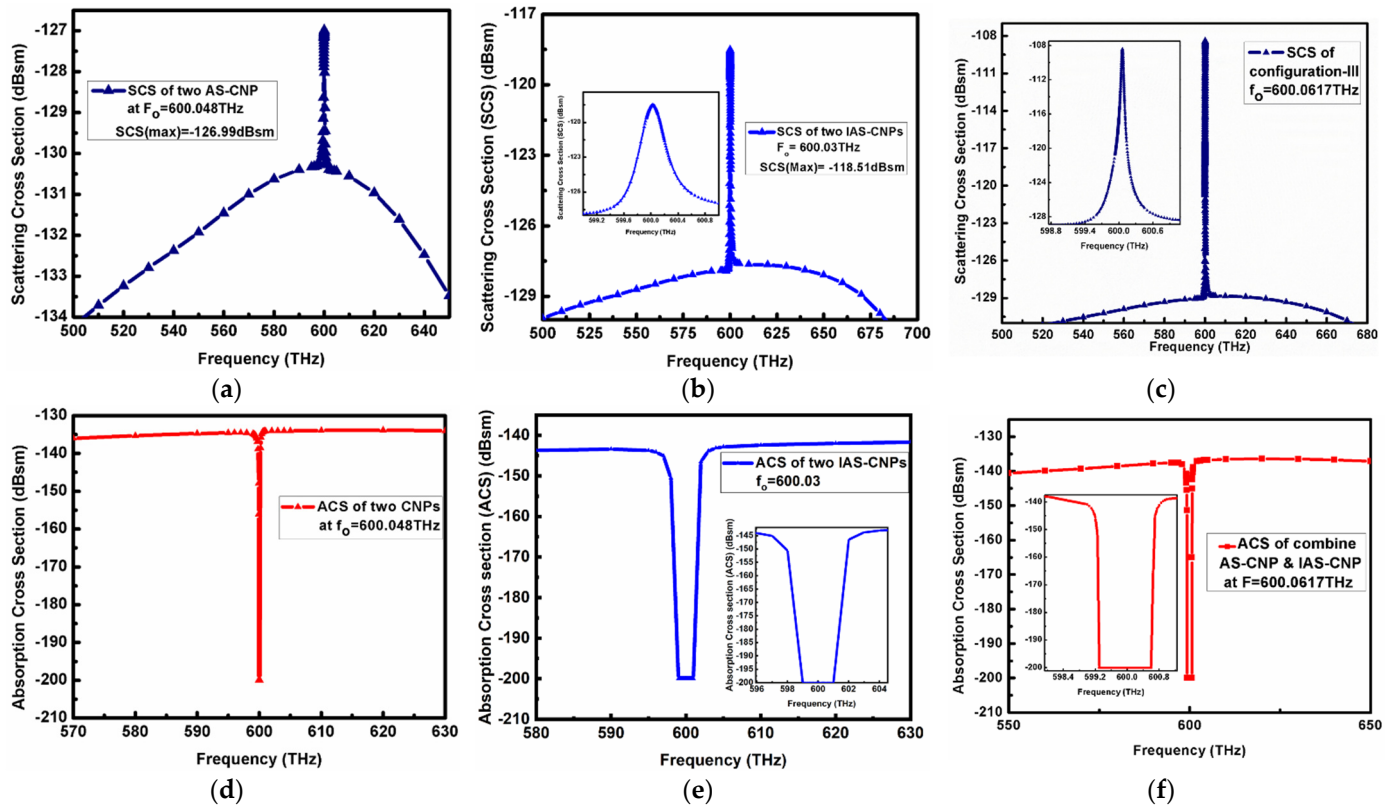


Figure 4. (a) Optimized SCS peaks for configuration I, (b) SCS peak for configuration II, (c) SCS peak for configuration III, (d) ACS for configuration I, (e) ACS for II and (f) ACS for configuration III at resonance frequency.

In case of configuration II, the inclusion of a passive dielectric does not affect the resonance peak of I-CNPs from the desired frequency. Therefore, configuration II does not need an optimization of parameters.

Similarly, in the case of configuration III, the parameters of CNP and I-CNP are the same as for configuration I and II, respectively.

4.1. SCS and ACS Comparison of the Three Configurations

Figure 4a reports $SCS = -126.99$ dBsm for configuration I at a frequency $f_0 = 600.048$ THz, which is 3.388 dB higher than the ground value. It is a decrease of 13.76 dB from the SCS of the single CNP, reported in Figure 2a. Likewise, Figure 4b shows maximum $SCS = -118.51$ dBsm at $f_0 = 600.03$ THz for configuration II. It is 9.26 dB higher than the ground value. In comparison with the single I-CNP model, it is almost similar to the SCS of the single I-CNP reported in Figure 3a. Despite this, the maximum SCS reported in Figure 4c is -108.6 dBsm for the third configuration, at $f_0 = 600.0617$ THz, which is 20.5 dB higher than the ground value.

It is noticeable that due to destructive coupling, the maximum SCS peaks reduce for the first two configurations as compared to the single CNP and I-CNP models, but for the desired configuration III, the SCS boosts. Moreover, the SCS for configuration III is 17.112 dB greater than the SCS of configuration I and 11.24 dB greater than configuration II. Adding to this, the minimum of ACSs for configurations I, II and III are 65, 55 and 60 dB below the background values reported in d, e and f, respectively.

4.2. Analysis of E-Field and Current Densities

Figure 5a–c illustrates the electric field of the three array configurations. The maximum values of the electric field for configurations I, II and III are 114 V/m, 25.1 V/m and 450 V/m, respectively, at their respective resonance frequencies. A clear coupling of the near E-field is observable in Figure 5a,b. On the other hand, the electric field for configuration III enhances to 450 V/m as shown in c. This configuration provides a large enhancement of electric fields because the selection of materials in the core and shell is articulated in such a way that the near-electric field of both individual formulations strengthens the electric field instead of the opposition.

Figure 5d–f represents the current densities of the three configurations. The maximum values for the current densities are 2.38×10^5 A/m², 3.97×10^5 A/m² and 18.7×10^5 A/m² for configurations I, II and III, respectively. By comparing the current densities of configurations I and II with their single CNP and I-CNP models, as shown in Figures 2c and 3c, the decline due to coupling is clear. Similarly, for configuration III, the current is stronger than configurations I and II, as well as from the individual CNP and I-CNP. From Figure 5f, the direction of the current in the I-CNP is directed from the silver in the core to the gain medium in the shell. In the CNP, it is directed from a gain medium in the core towards the silver in the shell, which strengthens the peak of the current density and corresponds to the electric field distribution in Figure 5c.

4.3. Analysis of Power Flow and Far-Field Pattern

Figure 6 reports the power flow and strong dipolar far-field pattern of the three configurations. Figure 6a–c reports the power flow for the three configurations as 0.89 VA/m², 0.243 VA/m² and 6.61 VA/m², respectively. In all configurations, power is pointing out from the gain media and flows towards the source. The power flow for the first two configurations decreases as compared to their single basic models due to coupling. The power flow for configuration III enhances almost five times as compared to the power flow of both configurations.

The far-field pattern in Figure 6d shows a 56.7 dBnm² scattering cross-section (SCS) for configuration I, which decreases by 10.5 dB from its single CNP model (as discussed in Figure 2f). Similarly, for the second configuration, the SCS is 65.5 dBnm², as shown in Figure 6e, which is a decrease of 3.4 dB gain from the single I-CNP model (described by Figure 3f). Figure 6f reports a 73.8 dBnm² SCS for configuration III. It is 17.1 dB and 8.3 dB higher than configuration I and II, respectively. It is also higher than the individual CNP and I-CNP.

For the far fields in Figure 6, the beam widths in the *xoz* plane are thinner in Figure 6d,e but fatter in f, which means that the directivities are larger for configurations I and II than that of configuration III. However, the peak values of the SCS in Figure 6d,e are smaller than that in Figure 6f. It is clear that the radiation efficiencies of configurations I and II are smaller than that of configuration III, which depends on the combination structure of configuration III.

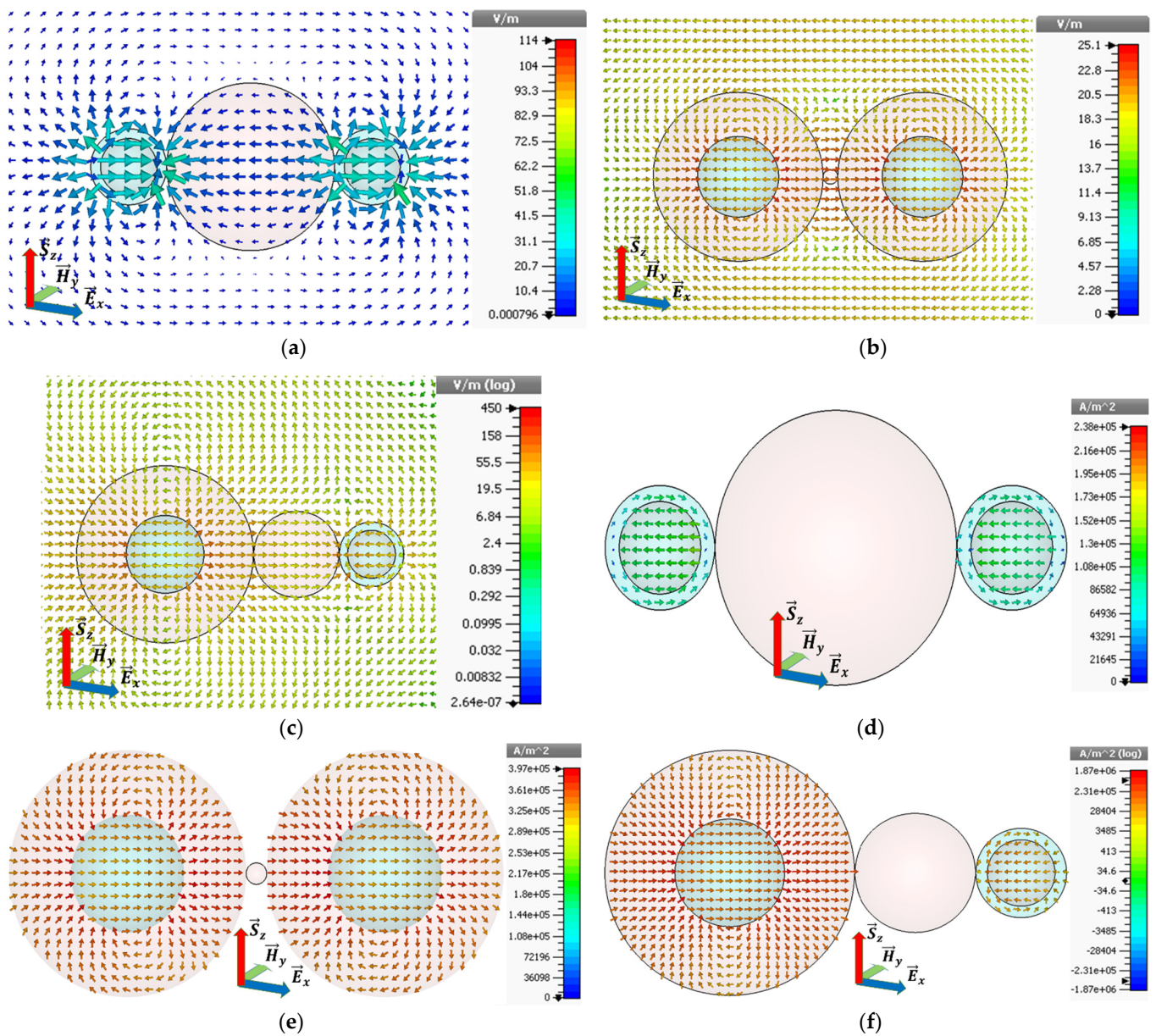


Figure 5. The electric fields of (a) configuration I (b) configuration II and (c) configuration III, respectively, at their respective resonance frequencies. Similarly, (d) shows electric current of configuration I, (e) shows configuration II and (f) shows configuration III, respectively, at their respective resonance frequencies.

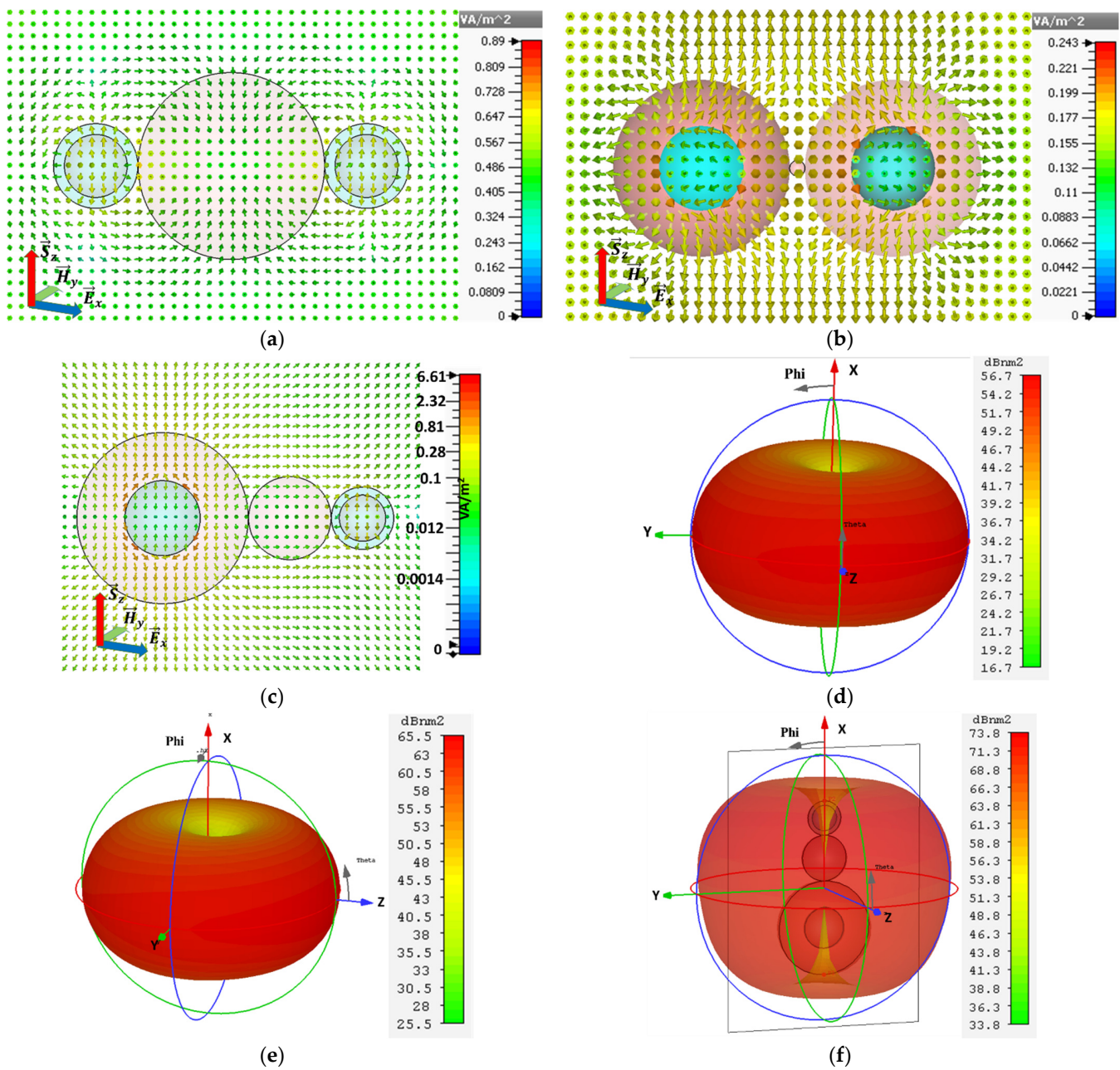


Figure 6. The power flow of (a) configuration I, (b) configuration II and (c) configuration III, whereas (d–f) show their far-field patterns at their resonance frequencies, respectively.

5. Analysis of the Benefits of Configuration III over I and II

From the results given in Section 4, it is clear that configuration III has overall better optical characteristics than configurations I and II. Table 2 gives the comparison of all these optical characteristics of the three configurations. The electric field enhances for configuration III due to the decrease in coupling, while it is restricted for configurations I and II. The decrease in power flow for configurations I and II is the evidence of higher destructive coupling of the electric field for these two configurations. However, the power flow for configuration III becomes enhanced almost six times greater than the other two configurations. Consequently, the SCS values for configuration III also increase by larger values than for configurations I and II. The RCS value of configuration III is 17 dB higher than that of configuration I and 8 dB higher than configuration II. With the above evidence, it is clear that configuration III is a more beneficial combination than the other two.

Table 2. The overall benefits of configuration III over configurations I and II.

	Thickness of Shell	Core Diameter	Frequency	SCS Max.	ACS below Background Values	SCS (Far-Field)	E field (Near Field) (Max.)	Power Flow (Max.)
Two active CNP	10 nm	58 nm	$f_0 = 600.048\text{THz}$	-126 dBsm	65 dBsm	56.7 dBnm ²	114 V/m	0.89 VA/m ²
Two Inverse Active CNPs	60 nm	94 nm	$f_0 = 600.03\text{THz}$	-118.51 dBsm	55 dBsm	65.5 dBnm ²	25 V/m	0.243 VA/m ²
Active CNP with Inverse CNP	Same as above for CNP and I-CNP	Same as above for CNP and I-CNP	$f_0 = 600.0617\text{THz}$	-108 dBsm	60 dBsm	73.8 dBnm ²	450 V/m	6.61 VA/m ²

6. Extension to Array Model

Here, we propose the arrangement of CNPs and I-CNPs for the formation of an array model in the presence of a passive dielectric medium, where the passive dielectric provides the stability to resonators as well as behaves as a capacitor to prevent losses of energy. The extension of the array model constitutes from repetitions of configuration III. Figure 7a shows the array model where the 10 nm silver shell enclosing the gain media in a core of diameter 58 nm constructs the active CNPs, whereas the 94 nm shell of gain media enclosing the silver in a core of a diameter of 60 nm forms the I-CNPs. The passive silica of diameter $L'_3 = 104\text{ nm}$ combines these CNPs and I-CNPs in rows. The passive dielectric also fills the separations of CNPs and I-CNPs in a column along the y-axis, which is $S = 0.64\lambda$. The \vec{E}_x polarized planewave propagating along the z-axis excites the array model.

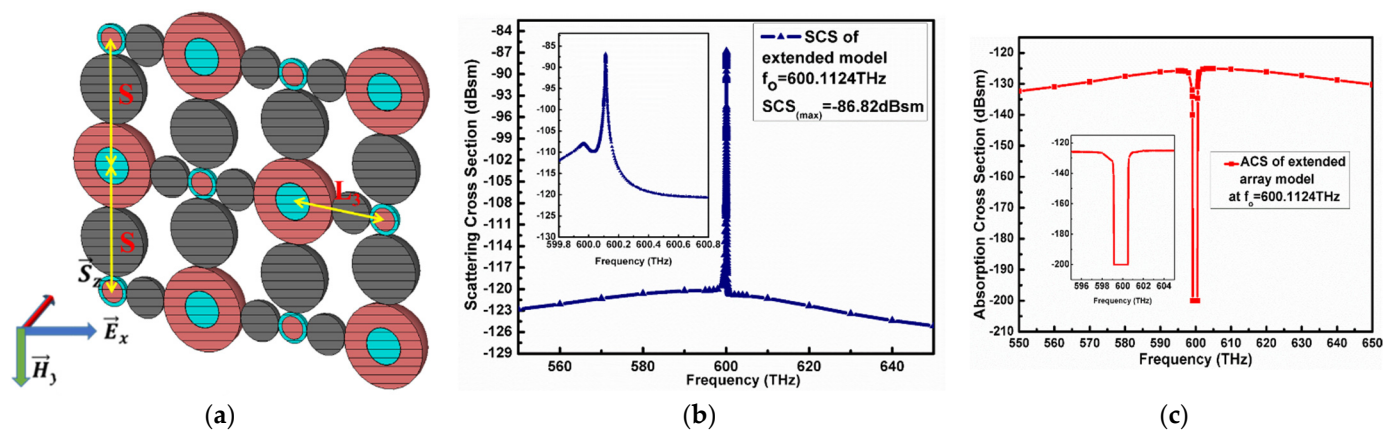


Figure 7. (a) Label diagram of extension of array model comprising both CNPs and I-CNPs; (b) scattering cross-section; (c) ACS of extended array model.

The maximum SCS obtained when the extended array radiates is $SCS = -86.82\text{ dBsm}$, which is nearly 35 dB higher than the background values and 23 dB higher than SCS reported for configuration III. Furthermore, the minimum of the ACS is 70 dB below the background values reported in Figure 7c.

The electric field and current density are shown in Figure 8a,b with peak values of 14477 V/m and $2.96 \times 10^7\text{ A/m}^2$, respectively, which increase more than 10 times of the single configuration III. Likewise, the power flow in Figure 8c enhances to 4799 VA/m², which is also an increase of more than 10 times as compared to single configuration III. In addition to this, the arrows denoting power flow in c are generating from gain media and project towards the source planewave direction. This direction of power flow is verified by the directive beam of the far-field pattern in Figure 8d, which points a maximum of 103 dBnm² gain along the z-axis, i.e., towards the source direction. The radiated electric field of the entire three rows of the model reports fewer coupling effects and gives highly directive-scattered radiation in the planewave direction instead of scattering in all directions.

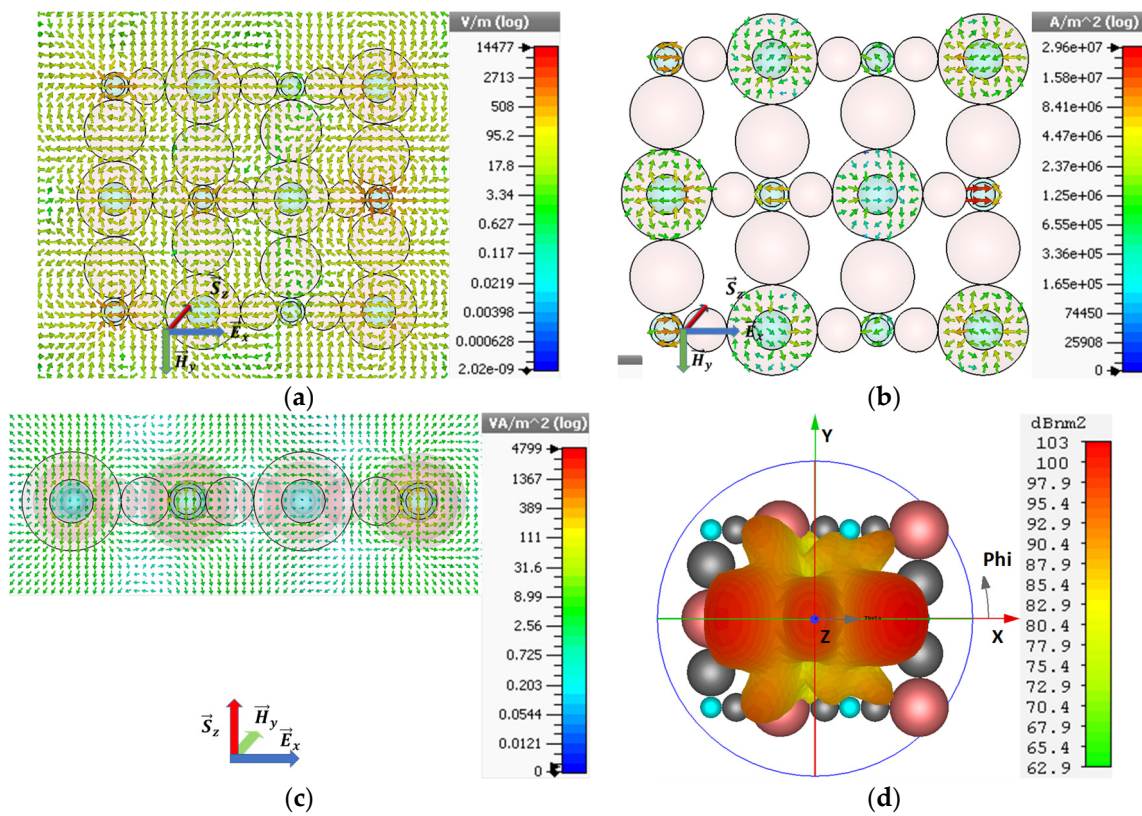


Figure 8. (a) Electric field spectrum, (b) current density, (c) power flow and (d) far-field pattern at the resonance frequency, respectively, for extended array model.

7. Comparison with Previous Work

Here, we are briefly comparing the scattering cross-section of the single and array models with the literature. Table 3 gives a brief comparison of the model reported here with the previously reported work. Here, this work provides another option, which can flexibly expand the array and realize high-performance transmission. It has a good application prospect in optical band communication, detection and so on.

Table 3. The comparison with previously reported arrays.

References	Type	SCS	Array SCS	Radiation Character
Ref [33]	CNPs including (Ag-SiO ₂)	−79.3817 dBsm	−78.3803 dBsm (for 12 particles)	Multipolar
Ref [29]	Core-Shell Cylinders (Ag-SiO ₂)	−120 dBsm	Not reported	Dipolar
This work	This article’s active CNP and I-CNP (Ag-SiO ₂)	−108 dBsm	−86.82 dBsm (for 6 particles)	Multipolar

8. Conclusions

An inverse active spherical coated nanoparticle (I-CNP) is designed and combined with a CNP for array formation to enhance the optical characteristics. Consequently, three different configurations of active core-shell nano-antennas were compared for optical characteristics. The electric field, radiated power, scattering cross-section and far-field gain for configurations I and II were reported as 114 V/m and 25 V/m, 0.89 VA/m² and 0.243 VA/m², −126 dBsm and −118 dBsm and 56.7 dBnm² and 65.5 dBnm², respectively,

whereas the enhancements in these optical parameters for the proposed array constitutes from configuration III are reported as 450 V/m, 6.61 VA/m², −108 dBsm and 73.8 dBnm², respectively. The results revealed that the configuration (III) having active spherical CNPs with their inverse active spherical CNPs shows the most suitable results, in comparison to that of the configurations that have two active spherical CNPs (I) or two inverse active spherical CNPs (II), due to tailoring with the core–shell material to reduce destructive coupling in the presence of small passive elements. Analysis demonstrates that the configuration of a CNP with its I-CNP separated by a passive dielectric can improve the optical characteristics and is worthy for nano-amplifier and nano-sensor applications.

Author Contributions: Conceptualization, Q.H.; Formal analysis, Q.H., C.R. and K.W.; Methodology, S.Y. and C.H.; Project administration, X.L.; Resources, A.U.R.; Software, Q.H.; Supervision, J.G. and R.J.; Writing—original draft, Q.H.; Writing—review & editing, H.Z. and J.L. All authors have read and agreed to the published version of the manuscript.

Funding: The National Natural Science Foundation of China sponsored this work under grant number 61571289.

Acknowledgments: The principle author would like to thank Junping Geng and Ronghong Jin for providing support in the entire research work and their precious suggestions in organizing this manuscript.

Conflicts of Interest: The authors declare no conflict of interest.

References

1. Bharadwaj, P.; Deutsch, B.; Novotny, L. Optical antennas. *Adv. Opt. Photon.* **2009**, *1*, 438–483. [[CrossRef](#)]
2. Jain, P.K.; Huang, X.; El-Sayed, I.H.; El-Sayed, M.A. Noble Metals on the Nanoscale: Optical and Photothermal Properties and Some Applications in Imaging, Sensing, Biology, and Medicine. *Acc. Chem. Res.* **2008**, *41*, 1578–1586. [[CrossRef](#)] [[PubMed](#)]
3. Catchpole, K.R.; Polman, A. Plasmonic solar cells. *Opt. Express* **2008**, *16*, 21793–21800. [[CrossRef](#)] [[PubMed](#)]
4. Maier, S.A. *Plasmonics: Fundamentals and Applications*; Springer Science & Business Media: New York, USA, 2007.
5. Xu, H. Plasmonic Nanowire Waveguide for Deep Subwavelength Confinement. In *Reviews in Plasmonics 2016*; Springer: Heidelberg, Germany, 2017; pp. 1–14.
6. Xi, Z.; Urbach, H. Magnetic dipole scattering from metallic nanowire for ultrasensitive deflection sensing. *Phys. Rev. Lett.* **2017**, *119*, 053902. [[CrossRef](#)]
7. Ozel, T.; Bourret, G.R.; Mirkin, C.A. Coaxial lithography. *Nat. Nanotechnol.* **2015**, *10*, 319–324. [[CrossRef](#)]
8. Ozel, T. Hybrid semiconductor core-shell nanowires with tunable plasmonic nanoantennas. In *Coaxial Lithography*; Springer: Cambridge, UK, 2016; pp. 27–41.
9. Ozel, T.; Ashley, M.J.; Bourret, G.R.; Ross, M.B.; Schatz, G.C.; Mirkin, C.A. Solution-dispersible metal nanorings with deliberately controllable compositions and architectural parameters for tunable plasmonic response. *Nano Lett.* **2015**, *15*, 5273–5278. [[CrossRef](#)]
10. Gordon, J.A.; Ziolkowski, R.W. Investigating functionalized active coated nanoparticles for use in nano-sensing applications. *Opt. Express* **2007**, *15*, 12562–12582. [[CrossRef](#)]
11. Lan, T.-H.; Tien, C.-H. Manipulation of the steering and shaping of SPPs via spatially inhomogeneous polarized illumination. *Opt. Express* **2010**, *18*, 23314–23323. [[CrossRef](#)]
12. Gordon, J.A.; Ziolkowski, R.W. Colors generated by tunable plasmon resonances and their potential application to ambiently illuminated color displays. *Solid State Commun.* **2008**, *146*, 228–238. [[CrossRef](#)]
13. Alkilany, A.M.; Thompson, L.B.; Boulos, S.P.; Sisco, P.N.; Murphy, C.J. Gold nanorods: Their potential for photothermal therapeutics and drug delivery, tempered by the complexity of their biological interactions. *Adv. Drug Deliv. Rev.* **2012**, *64*, 190–199. [[CrossRef](#)]
14. Wang, A.Z.; Langer, R.; Farokhzad, O.C. Nanoparticle delivery of cancer drugs. *Annu. Rev. Med.* **2012**, *63*, 185–198. [[CrossRef](#)]
15. Loo, C.; Lowery, A.; Halas, N.; West, J.; Drezek, R. Immunotargeted nanoshells for integrated cancer imaging and therapy. *Nano Lett.* **2005**, *5*, 709–711. [[CrossRef](#)]
16. Chen, J.; Wang, D.; Xi, J.; Au, L.; Siekkinen, A.; Warsen, A.; Li, Z.-Y.; Zhang, H.; Xia, Y.; Li, X. Immuno gold nanocages with tailored optical properties for targeted photothermal destruction of cancer cells. *Nano Lett.* **2007**, *7*, 1318–1322. [[CrossRef](#)]
17. Rejiya, C.; Kumar, J.; Raji, V.; Vibin, M.; Abraham, A. Laser immunotherapy with gold nanorods causes selective killing of tumour cells. *Pharmacol. Res.* **2012**, *65*, 261–269.
18. Yang, M.-D.; Liu, Y.-K.; Shen, J.-L.; Wu, C.-H.; Lin, C.-A.; Chang, W.H.; Wang, H.-H.; Yeh, H.-I.; Chan, W.-H.; Parak, W.J. Improvement of conversion efficiency for multi-junction solar cells by incorporation of Au nanoclusters. *Opt. Express* **2008**, *16*, 15754–15758. [[CrossRef](#)]
19. Cole, J.R.; Halas, N. Optimized plasmonic nanoparticle distributions for solar spectrum harvesting. *Appl. Phys. Lett.* **2006**, *89*, 153120. [[CrossRef](#)]

20. Zhang, F.; Braun, G.B.; Shi, Y.; Zhang, Y.; Sun, X.; Reich, N.O.; Zhao, D.; Stucky, G. Fabrication of Ag@SiO₂@Y₂O₃:Er Nanostructures for Bioimaging: Tuning of the Upconversion Fluorescence with Silver Nanoparticles. *J. Am. Chem. Soc.* **2010**, *132*, 2850–2851. [[CrossRef](#)]
21. Gordon, J.A.; Ziolkowski, R.W. CNP optical metamaterials. *Opt. Express* **2008**, *16*, 6692–6716. [[CrossRef](#)]
22. Rahman, A.U.; Geng, J.; Ziolkowski, R.W.; Hang, T.; Hayat, Q.; Liang, X.; Rehman, S.U.; Jin, R. Photoluminescence Revealed Higher Order Plasmonic Resonance Modes and Their Unexpected Frequency Blue Shifts in Silver-Coated Silica Nanoparticle Antennas. *Appl. Sci.* **2019**, *9*, 3000. [[CrossRef](#)]
23. Rahman, A.U.; Geng, J.; Rehman, S.U.; Hayat, K.; Liang, X.; Jin, R. Gap-Dependent Localized High Energy Multiple Dipolar Modes in Passive Silver-Coated Silica Nanoparticle Antennas. *Appl. Sci.* **2017**, *7*, 1183. [[CrossRef](#)]
24. Lombardi, A.; Grzelczak, M.P.; Crut, A.; Maioli, P.; Pastoriza-Santos, I.; Liz-Marzan, L.M.; Del Fatti, N.; Vallée, F. Optical response of individual Au–Ag@SiO₂ heterodimers. *ACS Nano* **2013**, *7*, 2522–2531. [[CrossRef](#)]
25. Xu, K.; Wang, J.-X.; Kang, X.-L.; Chen, J.-F. Fabrication of antibacterial monodispersed Ag–SiO₂ core–shell nanoparticles with high concentration. *Mater. Lett.* **2009**, *63*, 31–33. [[CrossRef](#)]
26. Liu, W.; Miroshnichenko, A.E.; Neshev, D.N.; Kivshar, Y.S. Broadband unidirectional scattering by magneto-electric core–shell nanoparticles. *ACS Nano* **2012**, *6*, 5489–5497. [[CrossRef](#)]
27. Liang, Z.; Susha, A.; Caruso, F. Gold nanoparticle-based core–shell and hollow spheres and ordered assemblies thereof. *Chem. Mater.* **2003**, *15*, 3176–3183. [[CrossRef](#)]
28. Yang, Y.; Hori, M.; Hayakawa, T.; Nogami, M. Self-assembled 3-dimensional arrays of Au@SiO₂ core-shell nanoparticles for enhanced optical nonlinearities. *Surf. Sci.* **2005**, *579*, 215–224. [[CrossRef](#)]
29. Geng, J.; Ziolkowski, R.W.; Jin, R.; Liang, X. Numerical Study of the Near-Field and Far-Field Properties of Active Open Cylindrical Coated Nanoparticle Antennas. *IEEE Photonics J.* **2011**, *3*, 1093–1110. [[CrossRef](#)]
30. Gordon, J.A.; Ziolkowski, R.W. The design and simulated performance of a coated nano-particle laser. *Opt. Express* **2007**, *15*, 2622–2653. [[CrossRef](#)]
31. Arslanagić, S.; Ziolkowski, R.W. Active coated nano-particle excited by an arbitrarily located electric Hertzian dipole—resonance and transparency effects. *J. Opt.* **2010**, *12*, 024014. [[CrossRef](#)]
32. Geng, J.; Chen, D.; Jin, R.; Liang, X.; Tang, J.; Ziolkowski, R.W. Study of active coated nano-toroid antennas. In Proceedings of the 2013 International Workshop on Antenna Technology (iWAT), Karlsruhe, Germany, 4–6 March 2013; pp. 154–157.
33. Hayat, Q.; Geng, J.; Liang, X.; Jin, R.; Ur Rehman, S.; He, C.; Wu, H.; Nawaz, H. Core-Shell Nano-Antenna Configurations for Array Formation with More Stability Having Conventional and Non-Conventional Directivity and Propagation Behavior. *Nanomaterials* **2021**, *11*, 99. [[CrossRef](#)]
34. Hayat, Q.; Geng, J.; Liang, X.; Jin, R.; Hayat, K.; He, C. Subwavelength plasmonic nanoantenna as a Plasmonic Induced Polarization Rotator (PI-PR). *Sci. Rep.* **2020**, *10*, 2809. [[CrossRef](#)]
35. Arslanagic, S.; Ziolkowski, R.W. Cylindrical and Spherical Active Coated Nanoparticles as Nanoantennas: Active Nanoparticles as Nanoantennas. *IEEE Antennas Propag. Mag.* **2017**, *59*, 14–29. [[CrossRef](#)]
36. Ghosh Chaudhuri, R.; Paria, S. Core/shell nanoparticles: Classes, properties, synthesis mechanisms, characterization, and applications. *Chem. Rev.* **2012**, *112*, 2373–2433. [[CrossRef](#)] [[PubMed](#)]
37. Lei, Y.; Chim, W.-K. Highly ordered arrays of metal/semiconductor core-shell nanoparticles with tunable nanostructures and photoluminescence. *J. Am. Chem. Soc.* **2005**, *127*, 1487–1492. [[CrossRef](#)] [[PubMed](#)]
38. Hayat, Q.; Geng, J.; Liang, X.; Jin, R.; He, C. Manipulation of Polarization Rotation through Spherical Active Coated Nanoparticle Antenna at Optical Wavelength. In Proceedings of the 2019 Photonics & Electromagnetics Research Symposium-Fall (PIERS-Fall), Xiamen, China, 17–20 December 2019; pp. 1015–1018.
39. Geng, J.; Ziolkowski, R.W.; Cambell, S.; Jin, R.; Liang, X. Studies of nanometer antennas incorporating gain material using CST. In Proceedings of the 2011 IEEE International Symposium on Antennas and Propagation (APSURSI), Spokane, WA, USA, 3–8 July 2011; pp. 1624–1627.